applied sciences

MDPI

Article

Dynamic Mechanical Behaviors of Desert Sand Concrete (DSC) after Different Temperatures

Minghu Zhang [1], Haifeng Liu [1,*], Shuai Sun [1], Xiaolong Chen [1] and Shu Ing Doh [2,*]

[1] College of Civil and Hydraulic Engineering, Ningxia University, Yinchuan 750021, China; shylock373@gmail.com (M.Z.); sswyyx0625@163.com (S.S.); 15009508105@163.com (X.C.)

[2] Faculty of Civil Engineering and Earth Resources, University Malaysia Pahang, Gambang 26300, Pahang, Malaysia

* Correspondence: liuhaifeng@nxu.edu.cn (H.L.); dohsi@ump.edu.my (S.I.D.); Tel.: +86-152-0268-3618 (H.L.)

Received: 3 September 2019; Accepted: 30 September 2019; Published: 3 October 2019

Featured Application: This paper applies to solve the shortage of building sand on the basis of principle of sustainable development. Meanwhile, this paper also provides guidance for desert sand concrete (DSC) subjected to elevated temperature and dynamic loading.

Abstract: In the building domain, the non-renewable resource of sand is widely used to produce concrete and mortar. The sand production has been estimated to be more than 10 billion tons with a total of 1.2 billion tons used in concrete in the last decade, which causes the gradual reduction of available building materials and impacts the environment. Since there are abundant desert sand resources in northwestern China, it would be viable to utilize desert sand as an alternative material for concrete production. In this study, an investigation of dynamic mechanical behaviors of desert sand concrete (DSC) was conducted. Various desert sand replacement ratios (0–100%) were used to replace the equivalent hill sand as fine aggregate. Experimental results showed that strain rate had a strong effect on the dynamic mechanical behaviors of DSC. The compressive strength (at room temperature) and flexural strength (after elevated temperature) increased with desert sand replacement ratio (DSRR) with the optimum replacement ratio of 40%, which was because the increase of DSRR improved the compaction of DSC. However, the effect of the low strength of desert sand was higher than that of the compaction when the DSSR exceeded 40%, so both strength values generally decreased with the increase of DSRR. Moreover, the dynamic constitutive model of DSC at room temperature was established on the basis of a nonlinear visco–elastic constitutive model (ZWT model), which can predict the stress–strain curves of DSC.

Keywords: desert sand concrete (DSC); dynamic compressive strength; dynamic flexural strength; deflection; strain rate; temperature

1. Introduction

Sand, defined as natural gravel deposit or crushed rock, is a non-renewable resource [1]. Sand is often used in concrete or mortar as fine aggregate and plays a significant role in building construction. However, high demand from the development of construction has required excessive sand over the years. The exploitable yield of river sand has exceeded 10 billion tons for the last decade [2], which causes threats to the environment. Therefore, it is crucial to identify alternative materials to reduce the dependency of non-renewable sand. Thus, locally available desert sand was used in this study. Chinese National Standard BJG19-65 [3] classifies fineness modulus of sand below 1.5 as superfine. The fineness modulus of desert sand, which ranges between 0.194 and 1.009 [4–7], was not frequently considered in concrete production due to its low workability.

Previous studies indicated the possible application of desert sand in concrete [1,4–6]. The workability of desert sand concrete (DSC) increased with the enhancement of desert sand replacement ratio (DSRR) up to 50% since the spheres shape of desert sand moved easier compared to angular or awkward shapes of particles [1,5]. The sand/cement ratio also had a significant effect on the workability of DSC. The desert sand filled the internal gap of concrete as the sand/cement ratio was below 1.14, which did not decrease the workability of DSC [4,6]. However, the workability reduced when the sand/cement ratio was over 1.14, because of the excess layer of water absorbed on the surface of desert sand. Thus, desert sand had a great workability under proper or suitable conditions.

Besides that, many studies have been carried out to investigate mechanical behaviors of DSC and mortar containing desert sand [1,6–15]. Conclusions differed with each other since region of desert sand or experimental conditions were different. The compressive strength and tensile strength of drying shrinkage cracking of concrete increased firstly, and then decreased with the enhancement of desert sand [7]. The increases of both strength values were because the compaction increased with the enhancement of DSRR. At the same time, the decreases of both strength values were because the round particles of desert sand decreased the cohesive force between coarse aggregate and grouts. Besides, both strength values had a maximum value when the DSRR was 20%. Meanwhile, the mechanical behaviors of concrete containing Mu Us desert sand (China) after elevated temperature (tensile splitting strength, axial compressive strength and elastic modulus) had the same trend with the enhancement of DSRR and reached the optimal value with DSRR of 40% [8,9]. However, the compressive strength, tensile strength, and static modulus of DSC gradually decreased with the increase of desert sand (Oman) [1]. This was because the increase on the surface of fine aggregate required more mortar to coat and the mortar of coating coarse aggregate decreased. Meanwhile, the maximum value of decrease of strength values was less than 15%. The 20% desert sand (Algeria) and 20% crushed sand, 60% desert sand (Tunisia), and 40% crushed sand could provide a great compressive strength for self-compacting concrete and concrete for pavement applications [10,11], respectively. The highest compressive strength of concrete containing Mu Us desert sand decreased by only 3% compared to that of plain concrete [12]. Besides, the optimal value of the water/cement ratio was 0.4. According to these above studies, it was feasible that desert sand was employed in concrete as fine aggregate. The improvement of feasibility may be due to different experimental conditions.

The current research mainly focused on the static mechanical behavior of DSC and mortar containing desert sand exposed to different temperatures. However, buildings may also subject to crash or impact loading during the period of service. The dynamic and static mechanical behaviors of concrete were different [16–24]. It was very limited for the research on the dynamic mechanical behavior of DSC. The effect of DSRR and impact velocity (5–30 m/s) on the mechanical behavior of DSC was tested and simulated. Meanwhile, the dynamic failure features of DSC were shown [25]. However, those just applied to high strain rate at room temperature. In fact, the range of strain rate is very wide, and DSC may be subjected to different temperatures, so many works require research to investigate these aspects.

In this paper, an electro–hydraulic servo universal testing machine was employed to investigate the dynamic compressive strength (at room temperature) and dynamic flexural strength (after elevated temperature) of DSC. The influence of DSRR and strain rate on the compressive strength of DSC at room temperature was investigated and the dynamic constitutive model was established to predict stress–strain curves of DSC. The relation between temperature, strain rate, DSRR, and flexural strength of DSC was also analyzed, which provided valuable information and guidance for the application of DSC in the building domain.

2. Experimental Program

2.1. Materials

Fine aggregate was composed of local hill sand and desert sand from Mu Us sandy land, respectively. Tables 1 and 2 list the physical behavior and chemical components of fine aggregate, respectively. As shown in Table 2, there were no toxic components and heavy metals in desert sand. Meanwhile, hill sand and desert sand had highly similar chemical components and physical behaviors. Using JGJ52-2006 criteria [26], the particle distribution of hill sand and desert sand are shown in Figure 1. It can be seen from Figure 1 that there was an obvious difference in particles for hill sand and desert sand. The vast majority of particles for desert sand were less than 0.15 mm. The fineness modulus of desert sand was 0.292 in this paper, which was only one eighth of hill sand. The particles of desert sand were much less than those of hill sand, which indicated that desert sand can greatly fill the internal gaps of concrete specimens produced with hill sand and desert sand. The current Chinese National Standards do not illustrate the utilization of desert sand in concrete. The 70% of crushed big stone (diameter of 10–20 mm) and 30% of small crushed stone (diameter of 5–10 mm) mixed together were utilized as coarse aggregate. These stones were purchased from a local stone material factory. Table 1 and Figure 1 also display physical behaviors and particle distribution of coarse aggregate (mixture of 10–20 mm and 5–10 mm stone), respectively.

Table 1. Physical behaviors of coarse and fine aggregate.

Aggregate Properties	Fine Aggregate		Coarse Aggregate
	Hill Sand	Desert Sand	Stone
apparent density (kg/m^3)	2636	2624	2698
bulk density (kg/m^3)	1567	1400	1430
void fraction (%)	41.6	40.95	47
mud content (%)	0.7	0.14	0.78
fineness modulus (%)	2.38	0.292	-
maximum particle (mm)	-	-	25
crush index (%)	-	-	8.6
content of needle-like particles (%)	-	-	9.5

Table 2. Chemical component of fine aggregate.

Chemical Component	Hill Sand (%)	Desert Sand (%)
SiO_2	86.55	82.66
FeO	0.98	1.85
Al_2O_3	9.74	8.72
CaO	0.96	2.00
MgO	1.09	1.51
K_2O	-	0.12
Na_2O	-	0.07
Loss on ignition	-	0.9

Ordinary Portland cement type 42.5 R from a local Saima cement factory was used. According to GB/T1346-2011 [27], the fineness and water consumption of standard consistency of cement were 4.7% (amount of residual 45 μm sieve) and 28%, respectively. The compressive strength at the age of 3 d and 28 d reached 33.5 MPa and 54.7 MPa, respectively. At the same time, the flexural strength at the age of 3 d and 28 d reached 6.7 MPa and 8.8 MPa, respectively. The initial time and final setting time were approximately 2 h 15 min and 2 h 54 min, respectively. Fly ash of Class I used in concrete as a cementitious material was produced by a local electric power plant, which conformed to GB/T1596-2017 [28]. The fineness, water content, SO_3 content, water requirement ratio, and loss on ignition of fly ash were 9.2%, 0.2%, 0.2%, 94%, and 2.8%, respectively.

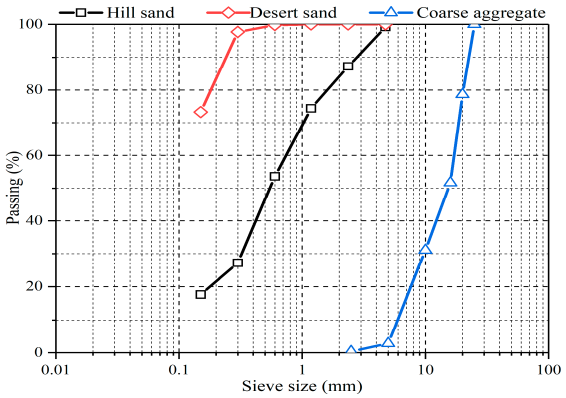

Figure 1. Particle distribution of coarse and fine aggregate.

Desert sand was characterized by small particles and large specific surface area, which easily caused DSC and mortar produced with desert sand to have high water demand and viscosity. The performance of DSC with admixture was better than that of DSC with no admixture [4]. Based on the above situation, a highly effective powder polycarboxylate superplasticizer supplied by Beijing Muhu Admixtures Co., Ltd. was used, which complied with JC/T223-2007 [29]. Tap water was utilized for concrete mixing and curing throughout the whole investigation.

2.2. Mix Proportions

In order to study the relation between DSRR and mechanical behaviors of concrete, various DSRR (0%, 20%, 40%, 60%, 80%, and 100%) used in specimens replaced the equivalent hill sand as fine aggregate. The water/cement ratio was 0.4. Previous research [30–32] indicated that the water/cement ratio of 0.39–0.4 was optimal in comparison with various water/cement ratios when the orthogonal test was performed to study the mechanical behaviors of concrete containing Mu Us desert sand. DSC specimens of Grade C50 were designed in this paper. Mixing proportion designed for the dynamic compressive test and four-point flexural test are described in Tables 3 and 4, respectively.

Table 3. Mixing proportion designed for dynamic compressive test. DSRR is desert sand replacement ratio.

Group	DSRR (%)	Quality of Materials (kg/m^3)					
		Water	Cement	Fine Aggregate		Coarse Aggregate	
				Hill Sand	Desert Sand	5–10 mm	10–20 mm
M1	0	195	488	530	0	371	866
M2	20	195	488	424	106	371	866
M3	40	195	488	318	212	371	866
M4	60	195	488	212	318	371	866
M5	80	195	488	106	424	371	866
M6	100	195	488	0	530	371	866

Table 4. Mixing proportion designed for dynamic four-point flexural test.

Group	Fly Ash Replacement Ratio (%)	DSRR (%)	Quality of Materials (kg/m^3)						
			Water	Cement	Fly Ash	Fine Aggregate		Coarse Aggregate	
						Hill Sand	Desert Sand	5–10 mm	10–20 mm
F1	0	0	195	488	0	549	0	350	818
F2	10	0	195	439	54	549	0	350	818
F3	20	0	195	390	107	549	0	350	818
F4		20	195	390	107	439	110	350	818
F5		40	195	390	107	329	220	350	818
F6		60	195	390	107	220	329	350	818
F7		80	195	390	107	110	439	350	818
F8		100	195	390	107	0	549	350	818

2.3. Specimen Preparation

Based on Tables 3 and 4, all raw experimental materials were strictly weighed by using an electric scale with the precision of 0.005 kg. In the mixing process, coarse and fine aggregate were placed into a forced mixer for 30 s mixing, and then cementitious materials were placed for 30 s mixing. Finally, in order to ensure the workability, superplasticizer, which was in powder form, was dissolved into water before and added into the mixer for 60 s of mixing. The dosage of required superplasticizer had to increase relatively to DSRR. This was due to the absorption feature of desert sand [1]. The absorption feature of DSC increased with the enhancement of DSRR. After the mixing process, compound concrete was put into plastic molds that were oiled in order to allow specimens to be demolded conveniently. Then, molds were vibrated on a vibration table for 2 min in order to decrease the internal gap and production of cracks. After casting in molds for 24 h, all specimens were demolded and then maintained for 28 d in the curing room at 18–22 °C and high relative humidity (above 95%).

Cubic specimens (100 mm × 100 mm × 100 mm) were produced to carry out the dynamic compressive test at room temperature, and prismatic specimens (100 mm × 100 mm × 100 mm) were used for the dynamic four-point flexural test after elevated temperature.

2.4. Experimental Methods

2.4.1. Dynamic Compressive Test at Room Temperature

Based on GB/T50081-2002 [33], all types of specimens were tested by a 1000 KN capacity electro–hydraulic servo universal testing machine (MTS) in different stress rates [34,35]. After 28 d, all specimens were taken out of the curing room and then placed in a laboratory (20 ± 2 °C) for 24 h to dry. According to the setting parameters of the instrument's software, all cubic specimens were tested at room temperature for the compressive strength in 0.05 MPa/s, 0.5 MPa/s, and 5 MPa/s, respectively. The elastic modulus was 34,500 N/mm^2 for concrete of grade C50 conforming to the GB50010-2010 [36], so stress rates of 0.05 MPa/s, 0.5 MPa/s, and 5 MPa/s were equal to the strain rates of 1.45×10^{-6} s^{-1}, 1.45×10^{-5} s^{-1}, and 1.45×10^{-4} s^{-1}, respectively. The higher the stress rate, the higher the strain rate. The experimental curves recorded by software were converted to stress–strain curves.

2.4.2. Dynamic Four-Point Flexural Test after Elevated Temperature

Before the heating process, all DSC prismatic specimens were dried in an oven at 85 °C for 24 h, which was to prevent specimens from spalling. Spalling is generally caused by high vapor pressure in the heating process [37]. DSC specimens were dried in an oven in order to reduce water content so that the vapor pressure was lower in the heating process than those without drying in the oven.

In the heating process, all prismatic specimens were heated to 300 °C, 500 °C, and 700 °C, respectively. The heating process was conducted with a heating furnace, which had an ultimate temperature of 1600 °C. The furnace system heated the DSC specimen to a predetermined temperature with a rate of 5 °C/min. Similar heating rate was also set by other researchers in previous studies [38–40]. Specimens maintained for 4 h after the DSC specimen reached the predetermined temperature in order to attain a thermal stable state, as described by previous studies [40,41]. The heating process of DSC specimen is shown in Figure 2. When the elevated temperature test was completed, DSC specimens were immediately removed out of oven to air cool and placed for 7 d in the laboratory (20 ± 2 °C). After that, the dynamic flexural strength of DSC was performed in a wide range of strain rates. The strain rate was defined as loading time divided by the ratio of dynamic flexural strength to the elastic modulus for concrete of grade C50 [36]. The stress rates applied at 0.01 MPa/s, 0.05 MPa/s, and 0.25 MPa/s corresponded to the strain rates of 3.57×10^{-7} s^{-1}, 2.16×10^{-6} s^{-1}, and 1.25×10^{-5} s^{-1}, respectively. Besides, the dial gauge was placed below the mid-span prismatic specimen. A camera was used to record the value of the dial gauge in the process of the experiment. According to the combination of video and experimental time–load curves of specimens, the value of the dial gauge in the moment of specimen failure could be obtained and then the value of deflection was known.

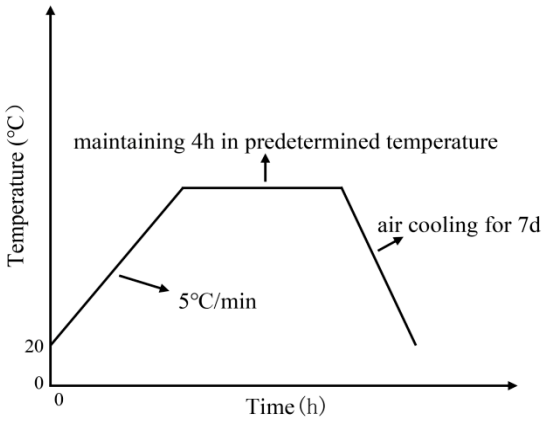

Figure 2. The heating process of desert sand concrete (DSC) specimen.

3. Mechanical Behaviors

3.1. Dynamic Compressive Strength and Dynamic Increase Factor (DIF) at Room Temperature

The strain rate of 1.45×10^{-6} s^{-1} was used as the quasi-static compressive test, while 1.45×10^{-5} s^{-1} and 1.45×10^{-4} s^{-1} were used as the dynamic compressive test. Six cubic specimens were produced in every case to ensure good reproducibility of experimental data, the average value of which was regarded as the experimental result. The quasi-static and dynamic compressive strength of results of DSC at room temperature are shown in Table 5. The dynamic compressive strength was the peak stress on the stress–strain curves of DSC.

Table 5. Quasi-static and dynamic compressive strength results of DSC at room temperature.

Strain Rate (s^{-1})	Compressive Strength Results of DSC at Room Temperature (MPa)					
	M1	**M2**	**M3**	**M4**	**M5**	**M6**
1.45×10^{-6}	53.3	57.1	54.1	48.6	54.7	49.5
	54.5	51.8	56.9	55.0	51.8	53.1
	54.0	57.5	57.2	56.8	52.0	50.4
average value	53.9	55.5	56.1	53.5	52.8	51.0
1.45×10^{-5}	55.1	59.1	59.3	56.3	55.1	54.1
	58.4	57.6	61.3	56.6	55.0	55.1
	53.7	58.2	57.4	56.4	57.5	56.7
average value	55.7	58.3	59.3	56.4	55.9	55.3
1.45×10^{-4}	63.0	64.1	63.1	63.9	59.9	59.0
	57.4	58.2	66.6	55.5	60.2	57.9
	58.9	65.0	63.8	64.6	60.2	57.5
average value	59.8	62.4	64.5	61.3	60.1	58.1

3.1.1. Influence of Strain Rate

The relation between strain rate and dynamic compressive strength of DSC at room temperature is presented in Figure 3. It can be clearly characterized in Table 5 and Figure 3 that strain rate had a strong effect on the dynamic compressive strength of DSC at room temperature. The dynamic compressive strength increased with the enhancement of strain rate at room temperature, which was in line with previous studies [34]. This phenomenon can be analyzed as follow: As a result of generation of new cracks and propagation of cracks, concrete specimens gradually appeared damage in the compressive process. The generation and propagation of cracks required consuming energy and the energy consumed for generation of cracks was far more than the propagation. The quantity of cracks increased with the enhancement of strain rate in the compressive process, which indicated that the

damage of specimens required lots of energy at a high strain rate. The compressive process spent an extremely short time at a high strain rate, but the compressive process with a short time could not accumulate enough energy to generate a great number of cracks. The only way to provide enough energy for arriving damage of specimen, is through improving the dynamic compressive strength of the concrete specimen [18,42,43].

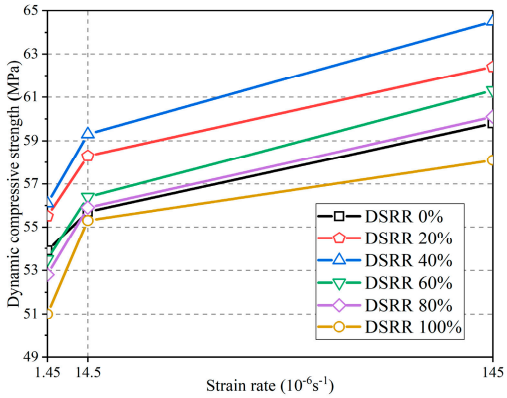

Figure 3. Relation between strain rate and dynamic compressive strength of DSC at room temperature.

For the sake of showing the effect degree of strain rate on the compressive strength of DSC at room temperature directly, dynamic increase factor (DIF) was defined as the ratio of dynamic compressive strength in different strain rates to the quasi-static compressive strength, which was widely used in dynamic analysis of concrete [18,25,42,44]. The DIF of DSC at room temperature with different DSRR is presented in Table 6 and described in Figure 4. As shown in Table 6 and Figure 4, the DIF increased with strain rate, which indicated DSC had a strain rate effect.

Table 6. Dynamic increase factor (DIF) of DSC at room temperature with different DSRR.

Strain Rate (s^{-1})	DIF					
	M1	**M2**	**M3**	**M4**	**M5**	**M6**
1.45×10^{-5}	1.033	1.050	1.057	1.054	1.059	1.084
1.45×10^{-4}	1.109	1.124	1.150	1.146	1.138	1.139

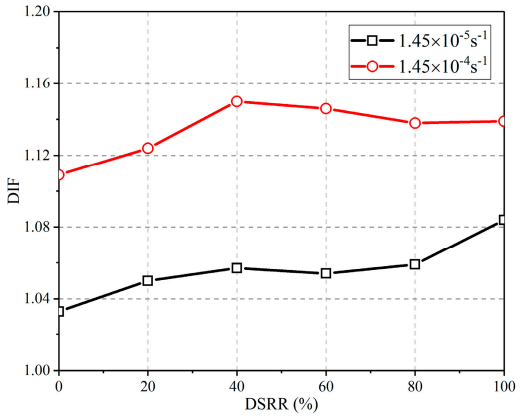

Figure 4. Relation between DIF and DSRR.

After the dynamic compressive test, the typical failure features of DSC M1 andM6 at different strain rates are shown in Figure 5. As displayed in Figure 5, DSC specimens created a failure shape with an hourglass-like profile in the dynamic compressive test with different strain rates. The production of an hourglass-like profile was due to the friction of the specimen up and down with steel plates in the compressive test. The DSC specimen gradually expanded with the increase of loading in the compressive test. However, the friction between specimens and steel plates up and down constrained the process of expansion. The effect of expansion decreased with the distance away from steel plates. Thus, the middle position of the DSC specimen, which was the minimum effect of friction, had severe damage [17]. The size of the hourglass-like profile became generally decreased with the strain rate, which indicated that the effect of expansion gradually increased with the strain rate. Moreover, it also can be found from Figure 5 that the size of the hourglass-like profile was gradually decreased with the increase of DSRR. This phenomenon was because the desert sand was characterized by small particles and less-angular appearance [45]. The less-angular appearance of desert sand indicated that desert sand easily rolled down after the compressive process. The rolling of desert sand produced fragments. As the enhancement of DSRR, the rolling amount of desert sand and fragments increased.

(**a**) $1.45 \times 10^{-6}\,s^{-1}$, M1 (**b**) $1.45 \times 10^{-5}\,s^{-1}$, M1 (**c**) $1.45 \times 10^{-4}\,s^{-1}$, M1

(**d**) $1.45 \times 10^{-6}\,s^{-1}$, M6 (**e**) $1.45 \times 10^{-5}\,s^{-1}$, M6 (**f**) $1.45 \times 10^{-4}\,s^{-1}$, M6

Figure 5. Typical failure features of DSC M1 and M6 at different strain rates.

On the other hand, the damage of DSC specimen was more severe with the increase of strain rate as shown in Figure 5. This phenomenon can be analyzed as follows: When the dynamic compressive strength of DSC specimen was tested at low strain rate, a small quantity of micro-cracks appeared and had adequate time to stretch until the failure of the specimen. Meanwhile, the interaction of micro-cracks was weak towards each other. Therefore, the damage of the DSC specimen was light, and the volume of fragments was large. At high strain rate, lots of micro-cracks performed propagations almost simultaneously since stress had a big increase rate in the compressive process, which caused micro-cracks to interact with each other strongly. Therefore, the damage of DSC specimens was severe, and the volume of fragments was small.

3.1.2. Influence of DSRR

The relation between DSRR and dynamic compressive strength of DSC at room temperature is presented in Figure 6. As displayed in Figure 6, the presence of desert sand significantly affected the change of compressive strength at room temperature. The compressive strength of DSC increased with the DSRR to an optimum value at 40%, and then dynamic compressive strength generally decreased with the DSRR when the DSRR was over 40%. This phenomenon can be analyzed as follow: The desert sand (superfine sand) and hill sand were employed in DSC. Desert sand was formed by the weathering of loose parent rocky and the strength of desert sand was lower than that of hill sand. Moreover, desert sand can fill internal gaps of DSC specimens due to its characteristic of tiny particles. In the first stage, the compaction of specimens continually increased with the enhancement of DSRR (0–40%), which

caused the increase of compressive strength. In the second stage, when the DSRR was over 40%, the low strength of desert sand had a higher effect on the compressive strength of DSC in comparison with the compaction. Therefore, the compressive strength of DSC decreased with the DSRR. The decrease of compressive strength of DSC at room temperature can be also explained by other mechanisms. The smooth surface and round shape of desert sand decreased the cohesive force of aggregate and grouts, which was responsible for the decrease of compressive strength [6,46]. The surface area of fine aggregate increased with the enhancement of DSRR due to the special characteristic of small particle. Therefore, more grouts were required to attach around fine aggregate, which caused the decrease of compressive strength of DSC at room temperature [1]. The highest compressive strength of DSC of grade C50 in 1.45×10^{-6} s^{-1}, 1.45×10^{-5} s^{-1}, and 1.45×10^{-4} s^{-1} were 2.2 MPa, 3.6 MPa, and 4.7 MPa, respectively, higher than those of DSC M1 (plain concrete). The lowest compressive strength decreased by 5.4% in comparison with those of DSC M1 at all strain rates, which indicated the compressive strength of DSC was similar to that of plain concrete.

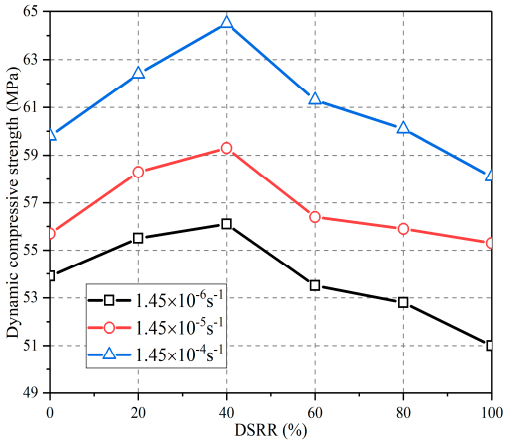

Figure 6. Relation between DSRR and the dynamic compressive strength of DSC at room temperature.

According to DIF, the effect degree of desert sand on the dynamic compressive strength of DSC can be also investigated. It is displayed in Figure 4 that the lowest DIF was reached when the DSRR was 0%. This phenomenon can be due to the effect of desert sand on the compaction of DSC. The addition of desert sand filled the internal gaps of DSC and increased the compaction. Therefore, the failure of DSC at room temperature required more energy than that of DSC with a DSRR of 0%.

3.1.3. Constitutive Model of DSC at Room Temperature

For the sake of describing stress–strain curves of DSC at room temperature, the constitutive model of DSC was developed on the basis of the ZWT model [47]. The ZWT model is a nonlinear visco–elastic constitutive model, which was widely applied to a great number of polymers or complex materials based on polymer, such as ethylene propylene diene monomer (EPDM) and polymer polymethylmethacrylate (PMMA) [48,49]. The rate-dependent damage constitutive model of steel–fiber concrete based on the ZWT model was investigated [50], which showed that the ZWT model was suitable to describe the constitutive behavior of steel–fiber concrete. Since then, this model has been universally utilized to describe the dynamic behaviors of concrete [42,44].

The ZWT model was formed by three parts in parallel: two Maxwell models presenting low strain rate and high strain rate, respectively, and a nonlinear elastic spring. The equation of the ZWT model is presented as follows:

$$\sigma = E_0\varepsilon + \alpha\varepsilon^2 + \beta\varepsilon^3 + E_1\int_0^\tau \dot{\varepsilon}e^{\left(-\frac{t-\tau}{\theta_1}\right)}d\tau + E_2\int_0^\tau \dot{\varepsilon}e^{\left(-\frac{t-\tau}{\theta_2}\right)}d\tau \quad (1)$$

where σ is stress; ε is strain; $\dot{\varepsilon}$ is strain rate; E_0 is Young's elastic modulus; and α and β represent material elastic constants, respectively. E_1 and θ_1 represent elastic modulus and relaxation time of visco–elastic response at low strain rate, respectively; E_2 and θ_2 represent elastic modulus and relaxation time of visco–elastic response at high strain rate, respectively; t represents experimental time; τ represents the time variable.

The value of θ_2 ranged from 10^{-4} to 10^{-6} s, and the experimental time of dynamic compression was far higher than θ_2. Visco–elastic response at high strain rate reached the slack status rapidly once the compressive experiment was conducted. Meanwhile, the value of $\dot{\varepsilon}$ was very small (10^{-6}–10^{-4} s^{-1}). Therefore, the visco–elastic response at high strain rate could be ignored. Moreover, the dynamic compressive test performed in a constant strain rate. Equation (1) can be simplified in the following form:

$$\sigma = E_0\varepsilon + \alpha\varepsilon^2 + \beta\varepsilon^3 + E_1\dot{\varepsilon}\theta_1\left[1 - e^{\left(-\frac{\varepsilon}{\dot{\varepsilon}\theta_1}\right)}\right]. \quad (2)$$

The compressive experiment of DSC with the strain rate of $1.45 \times 10^{-6}{\cdot}s^{-1}$ was regarded as the quasi-static compressive experiment. According to the least square method, the parameters of the constitutive model were fitted. The process of fitting can be divided into two parts. Firstly, the experimental curves at 1.45×10^{-5} s^{-1} were subtracted from those of 1.45×10^{-4} s^{-1} with the same DSRR. The pure elastic response of $E_0\varepsilon + \alpha\varepsilon^2 + \beta\varepsilon^3$ in Equation (2) was removed and then Equation (3) was obtained. Then, the unknown parameters of E_1 and θ_1 were fitted according to the least square method. Secondly, the values of E_1 and θ_1 were put into Equation (2) and the unknown values of E_0, α, and β were fitted according to curves of the static compressive experiment.

$$\sigma_2 - \sigma_1 = E_1\dot{\varepsilon}_2\theta_1\left[1 - e^{\left(-\frac{\varepsilon}{\dot{\varepsilon}_2\theta_1}\right)}\right] - E_1\dot{\varepsilon}_1\theta_1\left[1 - e^{\left(-\frac{\varepsilon}{\dot{\varepsilon}_1\theta_1}\right)}\right] \quad (3)$$

where σ_2 and $\dot{\varepsilon}_2$ are stress and strain rate at 1.45×10^{-4} s^{-1}, respectively; σ_1 and $\dot{\varepsilon}_1$ are stress and strain rate at 1.45×10^{-5} s^{-1}, respectively.

Through fitting with the ZWT model, parameters of the constitutive model of DSC with different DSRR at room temperature are presented in Table 7. The dynamic constitutive model of DSC was established when these parameters were put into Equation (2). Experimental curves and predicted curves of DSC at room temperature in different strain rates are shown in Figure 7. It is observed from Figure 7 that the experimental curves and predicted curves had high similarity, which indicates the ZWT model can greatly describe the stress−strain curve of DSC at room temperature.

Table 7. Parameters of the constitutive model of DSC with different DSRR at room temperature.

DSRR (%)	E_0 (MPa)	α	β	E_1 (MPa)	θ_1 (s)
0	4527	20,3861	-1.8×10^7	1660	121
20	4473	446,888	-3.4×10^7	1217	36
40	3050	441,877	-2.8×10^7	1339	790
60	4372	396,368	-3.2×10^7	960	1115
80	4778	252,518	-2.3×10^7	972	48
100	4011	395,576	-2.9×10^7	1711	46

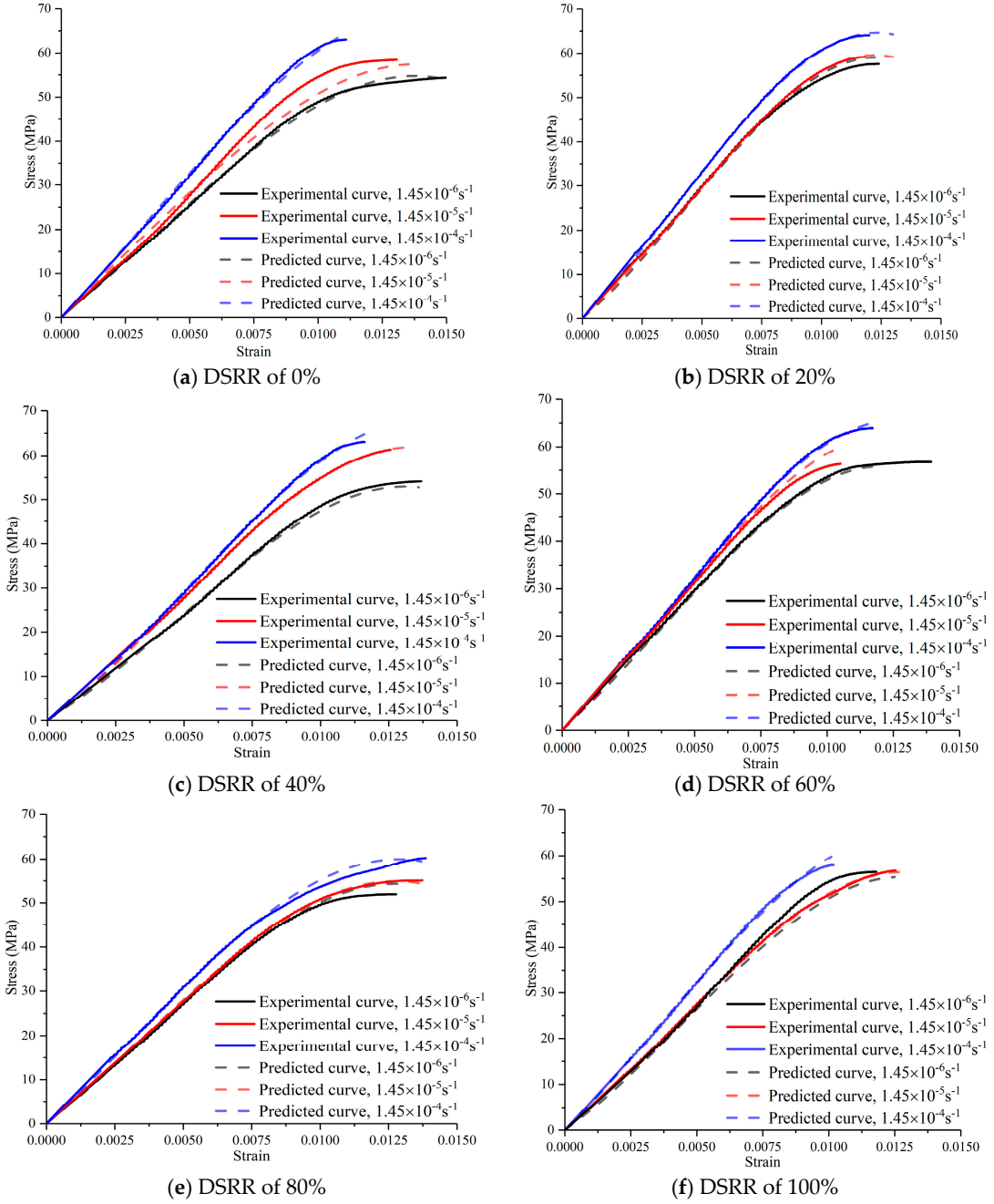

(**a**) DSRR of 0% (**b**) DSRR of 20%

(**c**) DSRR of 40% (**d**) DSRR of 60%

(**e**) DSRR of 80% (**f**) DSRR of 100%

Figure 7. Experimental curves and predicted curves of DSC at room temperature in various strain rates.

3.2. Dynamic Flexural Strength and Deflection after Elevated Temperature

3.2.1. Influence of Strain Rate

Prismatic specimens (100 mm × 100 mm × 400 mm) were used to test the flexural strength, which was frequently used as a significant index to evaluate the bending resistance of concrete beams. The dynamic flexural strength represented the behavior of concrete beam subjected to impact loading suddenly. Dynamic flexural strength results of DSC after elevated temperature are shown in Table 8. The relation between strain rate, flexural strength, and DSRR for DSC (F3–F8) is plotted in Figure 8. Six prismatic specimens were produced in every case and the value of Table 8 was the average value of experimental data. As displayed in Table 8 and Figure 8, the dynamic flexural strength increased with the enhancement of strain rate when DSC specimens were exposed to the same elevated temperature.

Table 8. Dynamic flexural strength results of DSC after elevated temperature

Group	Fly Ash Replacement Ratio (%)	DSRR (%)	Dynamic Flexural Strength Results of DSC after Elevated Temperature (MPa)								
			3.57×10^{-7} s^{-1}			2.16×10^{-6} s^{-1}			1.25×10^{-5} s^{-1}		
			300 °C	500 °C	700 °C	300 °C	500 °C	700 °C	300 °C	500 °C	700 °C
F1	0	0	2.44	1.11	0.44	2.75	1.34	0.64	3.01	1.36	0.72
F2	10	0	2.53	1.23	0.57	3.01	1.01	0.71	3.15	1.31	0.75
F3	20	0	2.49	1.17	0.54	2.92	1.27	0.60	3.10	1.33	0.69
F4		20	2.88	1.26	0.65	3.04	1.29	0.68	3.20	1.37	0.74
F5		40	3.16	1.32	0.68	3.34	1.64	0.98	3.42	1.70	1.05
F6		60	3.12	1.27	0.58	3.15	1.49	0.92	3.30	1.63	0.97
F7		80	2.90	1.24	0.50	3.12	1.40	0.86	3.24	1.53	0.88
F8		100	2.64	1.15	0.47	3.14	1.39	0.69	3.20	1.47	0.74

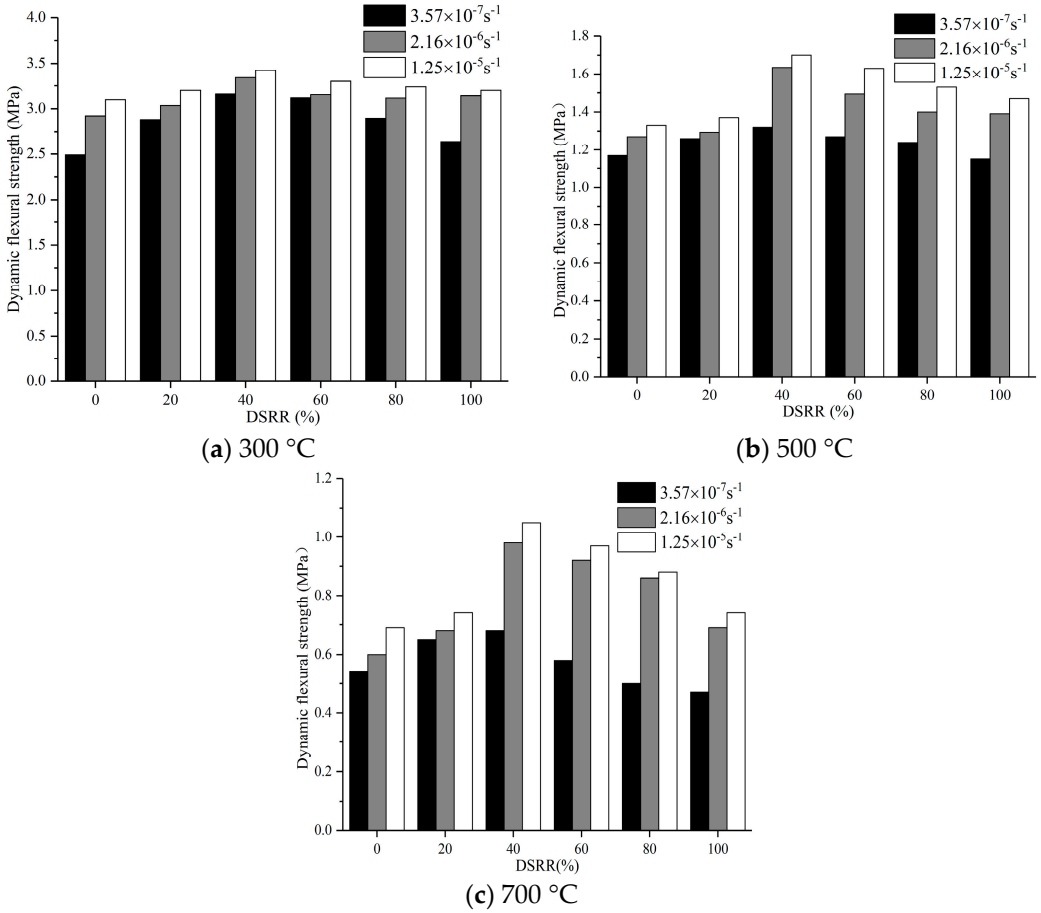

Figure 8. Relation between strain rate, flexural strength, and DSRR for DSC (F3–F8).

The vertical displacement of mid−span DSC was defined as the deflection measured by a dial gauge with the precision of 0.01 mm. The vertical deflection was used to evaluate the flexural toughness of DSC after elevated temperature, which represented the ability of vertical deformation of the DSC beam under loading. Dynamic deflection results of DSC after elevated temperature are shown in Table 9. It can be clearly found from Table 9 that the deflection of the DSC specimen after elevated temperature with the strain rate of 1.25×10^{-5} s^{-1} was much more than that of the specimen in 3.57×10^{-7} s^{-1}. For instance, deflections of DSC (F3−F8) with DSRR of 0%, 20%, 40%, 60%, 80%, and 100% after 300 °C in 1.25×10^{-5} s^{-1} increased by approximately 30%, 16.8%, 35%, 8.7%, 15.2%, and 14.3%, respectively, compared to those of specimens with the strain rate of 3.57×10^{-7} s^{-1}, which indicated that the deflection had a clear dependence of strain rate and increased with the enhancement of strain rate. This phenomenon may be analyzed as follow: The self−weight and flexural strength of DSC were responsible for the production of deflection. The self−weight and stiffness of DSC with the

same DSRR were almost alike after exposure to the same temperature, so the value of deflection was mainly determined by the flexural strength. It is observed from Figure 8 the flexural strength of DSC exposed to elevated temperature increased with strain rate. Therefore, the deflection increased with strain rate. Further, the flexural toughness increased as the strain rate rose.

Table 9. Deflection results of DSC after elevated temperature.

Group	Fly Ash Replacement Ratio (%)	DSRR (%)	Deflection Results of DSC after Elevated Temperature (mm)					
			3.57×10^{-7} s^{-1}			1.25×10^{-5} s^{-1}		
			300 °C	500 °C	700 °C	300 °C	500 °C	700 °C
F1	0	0	0.20	0.26	0.46	0.22	0.38	0.62
F2	10	0	0.23	0.29	0.43	0.27	0.33	0.52
F3	20	0	0.19	0.23	0.46	0.25	0.41	0.54
F4		20	0.22	0.26	0.30	0.26	0.32	0.37
F5		40	0.20	0.34	0.65	0.27	0.40	0.69
F6		60	0.23	0.29	0.57	0.25	0.35	0.71
F7		80	0.22	0.34	0.60	0.25	0.37	0.43
F8		100	0.21	0.32	0.55	0.24	0.34	0.61

3.2.2. Influence of DSRR

As shown in Table 8 (F3–F8) and Figure 8, there was a close relation between DSRR and the flexural strength of DSC after elevated temperature. As the DSRR increased, the dynamic flexural strength of DSC after elevated temperature produced a similar tendency to the compressive strength of DSC at room temperature (Figure 6). The flexural strength of DSC with the strain rate of 3.57×10^{-7} s^{-1} was taken as quasi−static flexural strength to analyze the tendency. Compared to the flexural strength of DSC with DSRR of 0%, the flexural strength of DSC with DSRR of 20%, 40%, 60%, 80%, and 100% after 300 °C increased about 15.7%, 26.9%, 25.3%, 16.3%, and 6.0%, respectively, while those of DSC after 500 °C increased about 7.7%, 12.8%, 8.5%, 6.0%, and 1.7%, respectively, and increased about 20.4%, 26.0%, 7.4%, −7.4%, and −13%, respectively, for those of DSC after 700 °C. These showed the flexural strength of DSC after elevated temperature increased firstly and then decreased with the DSRR. The highest flexural strength of DSC after elevated temperature was reached when the DSRR was 40%. It also can be seen from Table 8 (F3–F8) and Figure 8 that the overall flexural strength of DSC after elevated temperature was higher and the highest increase ratio reached 60%, compared to DSC with DSRR of 0%. This may be because the behavior of thermal expansion for hill sand was higher than that for desert sand. The volume of the concrete specimen appeared to have expanded after the heating process. The internal stress of the specimen increased with the enhancement of thermal expansion of sand. As the internal stress of the specimen increased, the flexural strength decreased.

3.2.3. Influence of Temperature

Flexural Strength and Deflection

The relation between temperature and flexural strength of DSC (F3–F8) with different strain rates is shown in Figure 9. As seen from Figure 9 and Table 8, the flexural strength of DSC F5, compared with those exposed to 300 °C, showed an obvious reduction of 58.2% and 78.5%, 51.5% and 70.7%, and 50% and 69.3% when DSC F5 were exposed to 500 °C and 700 °C with the strain rates of 3.57×10^{-7} s^{-1}, 2.16×10^{-6} s$^{-1,}$ and 1.25×10^{-5} s^{-1}, respectively. These analyses showed the flexural strength of DSC decreased with temperature. This phenomenon was because the calcium silicate hydrates (C−H−S) and calcium hydroxides ($Ca(OH)_2$) were decomposed with the temperature [51,52].

The relation between the temperature and deflection of DSC (F3–F8) is presented in Figure 10. It can be illustrated from Figure 10 that the deflection of DSC gradually increased with the temperature. As shown in Figure 10, the deflections of DSC F8 at 500 °C and 700 °C were greater than those of

300 °C: 52.4% and 41.7% for 500 °C, and 162% and 167% for 700 °C with the strain rate of 3.57×10^{-7} s^{-1} and 1.25×10^{-5} s^{-1}, respectively. This can be explained as follow: as the temperature increased, the evaporation and decomposition of grouts were gradually performed, which caused the decrease of compaction and increase of damage. The DSC of low compaction generated smaller deformation under a low impact loading in the four-point flexural test, compared to DSC with a high compaction. Moreover, the increase of damage decreased the stiffness of the DSC specimen. The increase of deflection also indicated that the failure gradually changed from brittle failure to plastic failure with the enhancement of temperature.

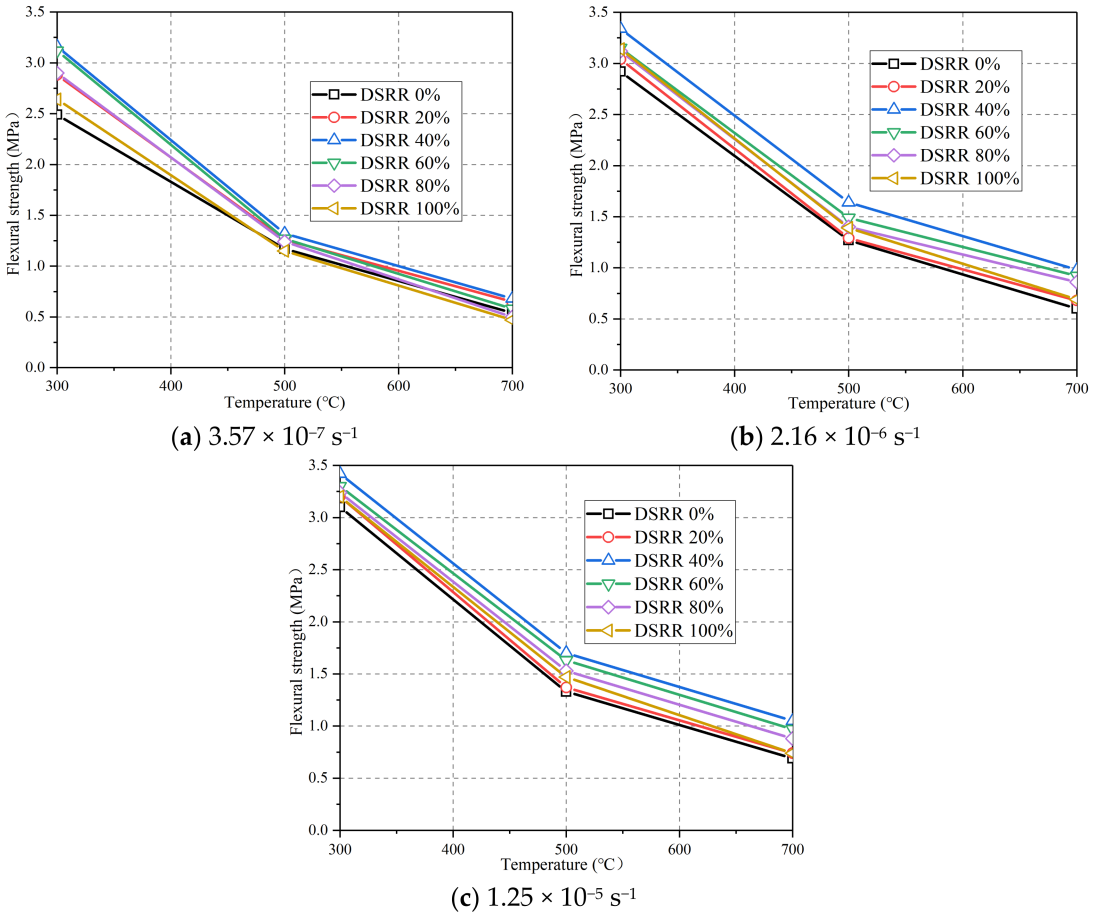

(**a**) 3.57×10^{-7} s^{-1} (**b**) 2.16×10^{-6} s^{-1}

(**c**) 1.25×10^{-5} s^{-1}

Figure 9. Relation between temperature and flexural strength of DSC (F3–F8) at different strain rate.

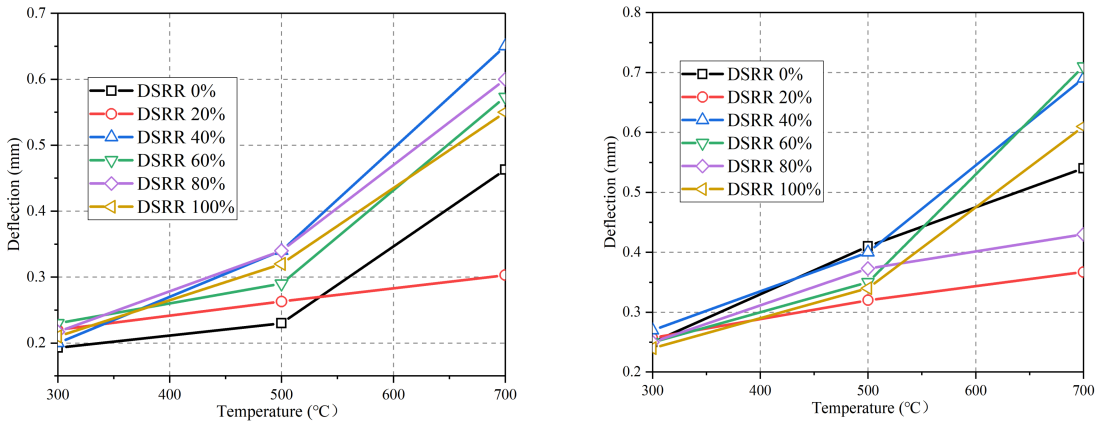

(**a**) 3.57×10^{-7} s^{-1} (**b**) 1.25×10^{-5} s^{-1}

Figure 10. Relation between the temperature and deflection of DSC (F3–F8) at different strain rate.

Apparent Appearance

Apparent appearance is a significant visual indicator for buildings exposed to elevated temperatures, which can preliminarily evaluate the degree of damage. Apparent appearance includes appearance of color, crack, and damage. The apparent appearances of DSC F5 after elevated temperature are shown in Figure 11.

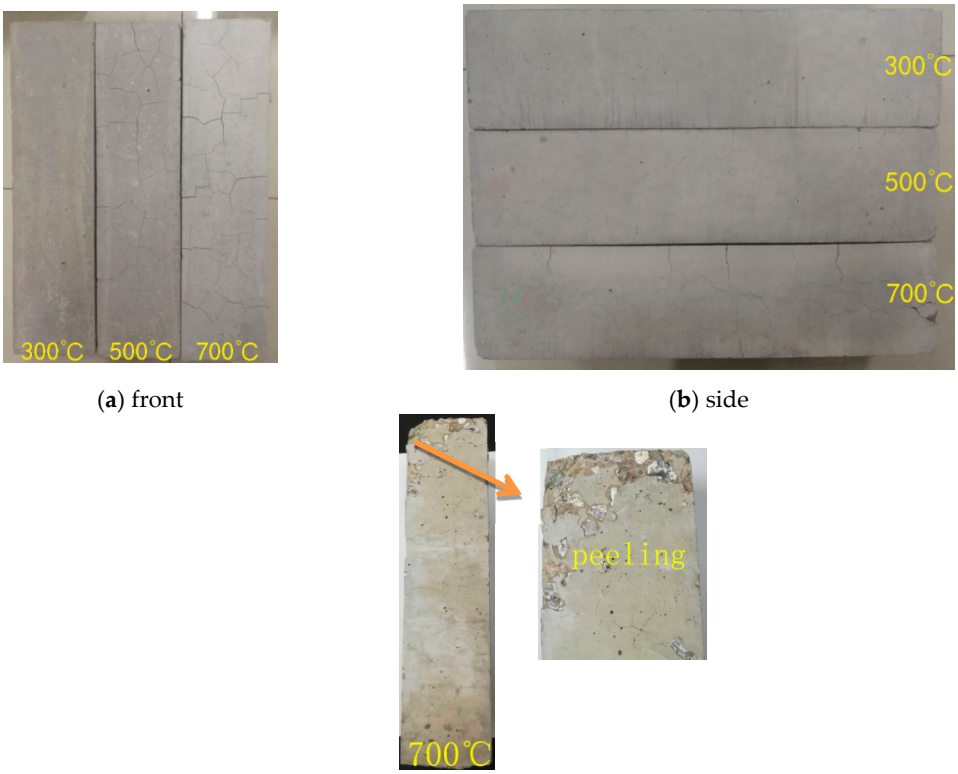

(**a**) front (**b**) side

(**c**) slight peeling on the surface of DSC specimen after 700 °C

Figure 11. Apparent appearances of DSC F5 after elevated temperature.

As shown in Figure 11a, the color of DSC specimen was dark grey and there were occurrences of some tiny cracks on the surface after 300 °C. Moreover, the impact sound was clunking. At 500 °C, the DSC specimen, with a slightly clear impact sound, turned into a light grey color and cracks became evident on the surface of the specimen. When the temperature went up to 700 °C, the color changed to light white and the width of cracks was larger. Besides, the impact sound turned to clear for DSC specimens. The change of color may be due to the effect of siliceous gravel. The siliceous gravel had many colors and the specimen showed different colors with different temperatures [53]. The different impact sounds were due to the change of compaction. The compaction of the DSC specimen decreased with the increase of temperature. Moreover, it is displayed in Figure 11b that the depth of cracks gradually increased on the surface of DSC specimens with temperature.

In a four-point flexural test, DSC specimens after 300 °C broke with a sudden loud sound of fracture while DSC specimens after 500 °C and 700 °C broke with a dull sound of fracture. This phenomenon may be because the compaction of the DSC specimen decreased with the enhancement of temperature. The elasticity gradually converted to elastic−plasticity for the DSC specimen.

Slight peeling appeared on the surface of DSC specimens after 700 °C, as shown in Figure 11c. This phenomenon can be explained as follow: the process of evaporation and decomposition of C−S−H occurred in DSC exposed to 700 °C [54,55], which weakened the relation between aggregate and grouts. Moreover, lime exposed to elevated temperature occurred with volume expansion [56]. The vaporization of the absorbed water led to the expansion of gaps; meanwhile, the structure of

grouts after elevated temperature became loose [57]. Therefore, the phenomenon of peeling appeared on the surface of the DSC specimen.

Weight Loss Rate

Every specimen was measured by electronic scale before and after the heating process. The electronic scale had an accuracy of 0.005 kg. To analyze the change of weight of DSC specimens exposed to elevated temperature, the weight loss rate was defined as:

$$\text{Weight loss rate } (\%) = \frac{m_2 - m_1}{m_1} \times 100 \quad (4)$$

where m_1 and m_2 are the weight of the DSC specimen exposed to elevated temperature before and after the heating process, respectively.

The weight loss rate of DSC exposed to elevated temperature is presented in Table 10. The weight loss rate of DSC continually went up with the increase of temperature as characterized from Table 10. For instance, the weight loss rates of DSC F5 after 300 °C, 500 °C, and 700 °C were 3.89%, 4.85%, and 6.77%, respectively. The reason for weight loss was the released water for DSC exposed to 300 °C [51,58]. Weight losses of DSC exposed to 500 °C and 700 °C were attributed to cement transformations such as its thermal decomposition [42,59]. Ordinary Portland cement (OPC) concrete above 450 °C experienced dehydration of C–H–S and the decomposition of $Ca(OH)_2$ [52].

Table 10. Weight loss rate of DSC after elevated temperature.

Group	Fly Ash Replacement Ratio (%)	DSRR (%)	Weight Loss Rate of DSC after Elevated Temperature (%)		
			300 °C	500 °C	700 °C
F1	0	0	2.67	3.56	4.96
F2	10	0	3.59	4.51	5.96
F3	20	0	4.27	5.51	6.73
F4		20	4.26	5.03	6.60
F5		40	3.89	4.85	6.77
F6		60	4.28	5.37	6.85
F7		80	4.14	5.27	6.69
F8		100	3.97	5.14	6.45

It also can be found from Table 10 that the weight loss rate increased with the enhancement of fly ash replacement ratio. The weight loss rate of DSC reached the maximum value when the fly ash replacement ratio amounted to 20%. This phenomenon may be caused by the decomposition of fly ash in elevated temperature.

4. Conclusions

This study investigated dynamic mechanical behaviors of DSC with different DSRR under the circumstance of room temperature and elevated temperature. According to the analysis of experimental results, the following conclusions were derived:

(1) The dynamic compressive strength at room temperature and flexural strength after elevated temperature increased with the DSRR to be optimum at 40% and both dynamic strength values generally decreased with the increase of DSRR after the DSRR was over 40%. The lowest compressive strength of DSC decreased by 5.4% in comparison with plain concrete in all strain rates.

(2) The dynamic flexural strength and deflection increased for DSC after elevated temperature with the enhancement of strain rate. The DIF and dynamic compressive strength obviously increased for DSC at room temperature with the enhancement of strain rate. The DIF of DSC was higher than that of plain concrete in every strain rate.

(3) The flexural strength decreased and deflection increased for DSC after elevated temperature with the enhancement of temperature.

(4) The dynamic constitutive model of DSC at room temperature was established on the basis of the nonlinear visco−elastic constitutive model (ZWT model), which can excellently predict the stress−strain curve for the dynamic compressive test.

Author Contributions: H.L. provided the idea and applied for funding to support this paper. S.S., M.Z. and X.C. performed these experiments. M.Z. contributed to the analysis of experiment data. M.Z. and H.L. wrote this paper. S.I.D. revised and put forward opinions for this paper.

Funding: This research was supported by National Natural Science Foundation of China (No.51368048, and 11162015) and Science Foundation of Ningxia (2018 AAC03030).

Conflicts of Interest: The authors declare no conflict of interest.

References

1. Al-Harthy, A.S.; Halim, M.A.; Taha, R.; Al-Jabri, K.S. The properties of concrete made with fine dune sand. *Constr. Build. Mater.* **2007**, *21*, 1803–1808. [CrossRef]
2. Liu, N. Study on the Mechanical Behavior of Desert Sand Concrete after High Temperature. Master's Thesis, Ningxia University, Yinchuan, China, 2018. (In Chinese)
3. Chinese Standard, B.J.G. *Preparation and Application Standard of Superfine Sand Concrete*; China Architecture and Building Press: Beijing, China, 1965. (In Chinese)
4. Zhang, G.X.; Song, J.X.; Yang, J.S.; Liu, X.Y. Performance of mortar and concrete made with a fine aggregate of desert sand. *Build. Environ.* **2006**, *41*, 1478–1481. [CrossRef]
5. Benabed, B.; Kadri, E.H.; Azzouz, L.; Kenai, S. Properties of self-compacting mortar made with various types of sand. *Cem. Concr. Compos.* **2012**, *34*, 1167–1173. [CrossRef]
6. Luo, F.J.; He, L.; Pan, Z.; Duan, W.H.; Zhao, X.L.; Collins, F. Effect of very fine particles on workability and strength of concrete made with dune sand. *Constr. Build. Mater.* **2013**, *47*, 131–137. [CrossRef]
7. Lee, E.; Park, S.; Kim, Y. Drying shrinkage cracking of concrete using dune sand and crushed sand. *Constr. Build. Mater.* **2016**, *126*, 517–526. [CrossRef]
8. Liu, H.F.; Liu, N. Influence of high temperature on the axis compressive strength and elastic modulus of desert sand concrete. *Bull. Chin. Ceram. Soc.* **2018**, *37*, 166–173. (In Chinese)
9. Sun, S.; Liu, H.F. Experimental research on the splitting tensile strength of desert sand concrete after high temperature. *Ind. Constr.* **2019**, *49*, 140–143. (In Chinese)
10. Douara, T.H.; Guettala, S. Effects of curing regimes on the physico-mechanical properties of self-compacting concrete made with ternary sands. *Constr. Build. Mater.* **2019**, *195*, 41–51. [CrossRef]
11. Khay, S.E.E.; Neji, J.; Loulizi, A. Compacted dune sand concrete for pavement applications. *Proc. Inst. Civ. Eng. Constr. Mater.* **2011**, *164*, 87–93. [CrossRef]
12. Jin, B.H.; Song, J.X.; Liu, H.F. Engineering characteristics of concrete made of desert sand from Maowusu Sandy Land. *Appl. Mech. Mater.* **2012**, *174*, 604–607. [CrossRef]
13. Seif, A.; Sedek, E.S. Performance of cement mortar made with fine aggregates of dune sand, Kharga Oasis, Western desert, Egypt: An experimental study. *Jordan J. Civ. Eng.* **2013**, *159*, 1–15.
14. Rmili, A.; Ben Ouezdou, M.; Added, M.; Ghorbel, E. Incorporation of crushed sands and Tunisian desert sands in the composition of self compacting concretes part I: Study of formulation. *Int. J. Concr. Struct. Mater.* **2009**, *3*, 3–9. [CrossRef]
15. Bouziani, T.; Bederina, M.; Hadjoudja, M. Effect of dune sand on the properties of flowing sand-concrete (FSC). *Int. J Concr. Struct. Mater.* **2012**, *6*, 59–64. [CrossRef]
16. Cao, S.; Hou, X.; Rong, Q.; Zheng, W.; Abid, M.; Li, G. Effect of specimen size on dynamic compressive properties of fiber-reinforced reactive powder concrete at high strain rates. *Constr. Build. Mater.* **2019**, *194*, 71–82. [CrossRef]
17. Guo, Y.B.; Gao, G.F.; Jing, L.; Shim, V.P.W. Response of high-strength concrete to dynamic compressive loading. *Int. J. Impact Eng.* **2017**, *108*, 114–135. [CrossRef]

18. Zhang, H.; Wang, L.; Zheng, K.; Bakura, T.J.; Totakhil, P.G. Research on compressive impact dynamic behavior and constitutive model of polypropylene fiber reinforced concrete. *Constr. Build. Mater.* **2018**, *187*, 584–595. [CrossRef]
19. Hou, X.; Cao, S.; Rong, Q.; Zheng, W.; Li, G. Effects of steel fiber and strain rate on the dynamic compressive stress-strain relationship in reactive powder concrete. *Constr. Build. Mater.* **2018**, *170*, 570–581. [CrossRef]
20. Al-Salloum, Y.; Almusallam, T.; Ibrahim, S.M.; Abbas, H.; Alsayed, S. Rate dependent behavior and modeling of concrete based on SHPB experiments. *Cem. Concr. Compos.* **2015**, *55*, 34–44. [CrossRef]
21. Li, N.; Long, G.; Fu, Q.; Song, H.; Ma, C.; Li, H. Dynamic mechanical characteristics of filling layer self-compacting concrete under impact loading. *Arch. Civ. Mech. Eng.* **2019**, *19*, 851–861. [CrossRef]
22. He, Y.M.; Huo, J.S. Impact tests on dynamic behavior of concrete at elevated temperatures. *J. Eng. Mech.* **2012**, *29*, 200–208. (In Chinese)
23. Li, Z.; Xu, J.; Bai, E. Static and dynamic mechanical properties of concrete after high temperature exposure. *J. Mater. Sci. Eng. A* **2012**, *544*, 27–32. [CrossRef]
24. Chen, L.; Fang, Q.; Jiang, X.; Ruan, Z.; Hong, J. Combined effects of high temperature and high strain rate on normal weight concrete. *Int. J. Impact Eng.* **2015**, *86*, 40–56. [CrossRef]
25. Liu, H.F.; Ma, J.R.; Wang, Y.Y.; Ning, J.G. Influence of desert sand on the mechanical properties of concrete subjected to impact loading. *Acta Mech. Solida Sin.* **2017**, *30*, 583–595.
26. Chinese Standard JGJ52-2006. *Standard for Technical Requirements and Test Method of Sand and Crushed Stone (or Gravel) for Ordinary Concrete*; China Architecture and Building Press: Beijing, China, 2006. (In Chinese)
27. Chinese Standard GB/T1346-2011. *Test Methods for Water Requirement of Normal Consistency, Setting Time and Soundness of the Portland Cement*; Standards Press of China: Beijing, China, 2011. (In Chinese)
28. Chinese Standard GB/T1596-2017. *Fly Ash Used for Cement and Concrete*; Standards Press of China: Beijing, China, 2017. (In Chinese)
29. Chinese Standard JC/T223-2007. *Polycarboxylates High Performance Water—Reducing Admixture*; Standards Press of China: Beijing, China, 2007. (In Chinese)
30. Du, Y.G.; Liu, H.F.; Ma, H.J.; Liu, N. Experiment on the compressive and flexural strength of desert sand concrete. *Concrete* **2018**, 102–104. (In Chinese)
31. Lv, J.B.; Liu, N.; Liu, H.F. Study on the compressive strength of desert sand concrete after elevated temperature. *Concrete* **2017**, 129–133. (In Chinese)
32. Ma, H.J. Study on Carbonization Resistance and Resistance to Chloride ion Permeability of Desert Sand Concrete. Master's Thesis, Ningxia University, Yinchuan, China, 2018. (In Chinese)
33. Chinese Standard GB/T50081-2002. *Standard for Test Method of Mechanical Properties on Ordinary Concrete*; Standards Press of China: Beijing, China, 2017. (In Chinese)
34. Xiao, J.; Li, Z.; Xie, Q.; Shen, L. Effect of strain rate on compressive behaviour of high-strength concrete after exposure to elevated temperatures. *Fire Saf. J.* **2016**, *83*, 25–37. [CrossRef]
35. Mirmomeni, M.; Heidarpour, A.; Zhao, X.L.; Packer, J.A. Effect of elevated temperature on the mechanical properties of high-strain-rate-induced partially damaged concrete and CFSTs. *Int. J. Impact Eng.* **2017**, *110*, 346–358. [CrossRef]
36. Chinese Standard GB50010-2010. *Starndard for Design of Concrete Structures*; China Architecture and Building Press: Beijing, China, 2002. (In Chinese)
37. Halicka, A.; Ogrodnik, P.; Zegardlo, B. Using ceramic sanitary ware waste as concrete aggregate. *Constr. Build. Mater.* **2013**, *48*, 295–305. [CrossRef]
38. Gupta, T.; Siddique, S.; Sharma, R.K.; Chaudhary, S. Effect of elevated temperature and cooling regimes on mechanical and durability properties of concrete containing waste rubber fiber. *Constr. Build. Mater.* **2017**, *137*, 35–45. [CrossRef]
39. Chan, S.Y.N.; Luo, X.; Sun, W. Effect of high temperature and cooling regimes on the compressive strength and pore properties of high performance concrete. *Constr. Build. Mater.* **2000**, *14*, 261–266. [CrossRef]
40. Kou, S.C.; Poon, C.S.; Etxeberria, M. Residue strength, water absorption and pore size distributions of recycled aggregate concrete after exposure to elevated temperatures. *Cem. Concr. Compos.* **2014**, *53*, 73–82. [CrossRef]
41. Wang, H.Y. The effects of elevated temperature on cement paste containing GGBFS. *Cem. Concr. Compos.* **2008**, *30*, 992–999. [CrossRef]

42. Zhang, H.; Wang, B.; Xie, A.; Qi, Y. Experimental study on dynamic mechanical properties and constitutive model of basalt fiber reinforced concrete. *Constr. Build. Mater.* **2017**, *152*, 154–167. [CrossRef]
43. Zhang, H.; Liu, Y.; Sun, H.; Wu, S. Transient dynamic behavior of polypropylene fiber reinforced mortar under compressive impact loading. *Constr. Build. Mater.* **2016**, *111*, 30–42. [CrossRef]
44. Dong, S.; Han, B.; Yu, X.; Ou, J. Dynamic impact behaviors and constitutive model of super-fine stainless wire reinforced reactive powder concrete. *Constr. Build. Mater.* **2018**, *184*, 602–616. [CrossRef]
45. Che, J.L.; Wang, D.; Liu, H.F.; Zhang, Y.X. Mechanical properties of desert sand-based fiber reinforced concrete (DS-FRC). *Appl. Sci.* **2019**, *9*, 1–18. [CrossRef]
46. Monteiro, P. *Concrete: Microstructure, Properties, and Materials*; McGraw-Hill Publishing: New York, NY, USA, 2006.
47. Wang, L.; Shi, S.; Chen, J.; Huang, D. Research and application of constitutive relation of nonlinear thermal visco-elastic about ZWT model. *J. Ningbo Univ. Nat. Sci. Eng. Ed.* **2002**, *15*, 141–149. (In Chinese)
48. Jiang, J.; Xu, J.; Zhang, Z.; Chen, X. Rate-dependent compressive behavior of EPDM insulation: Experimental and constitutive analysis. *Mech. Mater.* **2016**, *96*, 30–38. [CrossRef]
49. Dar, U.A.; Zhang, W.; Xu, Y. Numerical implementation of strain rate dependent thermo visco-elastic constitutive relation to simulate the mechanical behavior of PMMA. *Int. J. Mech. Mater. Des.* **2014**, *10*, 93–107. [CrossRef]
50. Huang, X.; Chen, J.; Wang, L. The dynamic constitutive relation of concrete made of SFRC. *J. Sichuan Univ. Sci. Technol.* **2003**, *22*, 80–82. (In Chinese)
51. Savva, A.; Manita, P.; Sideris, K.K. Influence of elevated temperatures on the mechanical properties of blended cement concretes prepared with limestone and siliceous aggregates. *Cem. Concr. Compos.* **2005**, *27*, 239–248. [CrossRef]
52. Awal, A.S.M.A.; Shehu, I.A.; Ismail, M. Effect of cooling regime on the residual performance of high-volume palm oil fuel ash concrete exposed to high temperatures. *Constr. Build. Mater.* **2015**, *98*, 875–883. [CrossRef]
53. Annerel, E.; Taerwe, L. Revealing the temperature history in concrete after fire exposure by microscopic analysis. *Cem. Concr. Res.* **2009**, *39*, 1239–1249. [CrossRef]
54. Khoury, G.A.; Grainger, B.N.; Sullivan, P.J.E. Transient thermal strain of concrete: Literature review, conditions within specimen and behavior of individual constituents. *Mag. Concr. Res.* **1985**, *37*, 131–144. [CrossRef]
55. Peng, G.F. Evaluation of Fire Damage to High Performance Concrete. Doctoral Dissertation, Hong Kong Polytechnic University, Hong Kong, China, 1999.
56. Lin, W.M.; Lin, T.D.; Powers-Couche, L.J. Microstructures of fire-damaged concrete. *Mater. J.* **1996**, *93*, 199–205.
57. Karakoç, M.B. Effect of cooling regimes on compressive strength of concrete with lightweight aggregate exposed to high temperature. *Constr. Build. Mater.* **2013**, *41*, 21–25. [CrossRef]
58. Ramanchanfran, V.S.; Feldman, R.F.; Beaudoin, J.J. *Concrete Science, Treatise on Current Research*; Heyden and Son Ltd.: London, UK, 1981.
59. Ismail, M.; Ismail, M.E.G.; Muhammad, B. Influence of elevated temperatures on physical and compressive strength properties of concrete containing palm oil fuel ash. *Constr. Build. Mater.* **2011**, *25*, 2358–2364. [CrossRef]